University of Groningen

Bubble splitting under gas–liquid–liquid three-phase flow in a double T-junction microchannel

Liu, Yanyan; Yue, Jun; Zhao, Shuainan; Yao, Chaoqun; Chen, Guangwen

Published in:
AIChE Journal

DOI:
10.1002/aic.15920

IMPORTANT NOTE: You are advised to consult the publisher's version (publisher's PDF) if you wish to cite from it. Please check the document version below.

Document Version
Final author's version (accepted by publisher, after peer review)

Publication date:
2018

Link to publication in University of Groningen/UMCG research database

Citation for published version (APA):
Liu, Y., Yue, J., Zhao, S., Yao, C., & Chen, G. (2018). Bubble splitting under gas–liquid–liquid three-phase flow in a double T-junction microchannel. *AIChE Journal*, *64*(1), 376-388. https://doi.org/10.1002/aic.15920

Copyright
Other than for strictly personal use, it is not permitted to download or to forward/distribute the text or part of it without the consent of the author(s) and/or copyright holder(s), unless the work is under an open content license (like Creative Commons).

Take-down policy
If you believe that this document breaches copyright please contact us providing details, and we will remove access to the work immediately and investigate your claim.

Downloaded from the University of Groningen/UMCG research database (Pure): http://www.rug.nl/research/portal. For technical reasons the number of authors shown on this cover page is limited to 10 maximum.

Download date: 23-11-2020

Bubble splitting under gas-liquid-liquid three-phase flow in a double T-junction microchannel

Yanyan Liu[1,3], Jun Yue[2], Shuainan Zhao[1], Chaoqun Yao[1*] and Guangwen Chen[1*]

1. Dalian National Laboratory for Clean Energy, Dalian Institute of Chemical Physics, Chinese Academy of Sciences, Dalian 116023, China

2. Department of Chemical Engineering, Engineering and Technology Institute Groningen, University of Groningen, 9747 AG Groningen, The Netherlands

3. University of Chinese Academy of Sciences, Beijing 100049, China

Abstract

Gas-aqueous liquid-oil three-phase flow was generated in a microchannel with a double T-junction. Under the squeezing of the dispersed aqueous phase at the second T-junction (T2), the splitting of bubbles generated from the first T-junction (T1) was investigated. During the bubble splitting process, the upstream gas-oil two-phase flow and the aqueous phase flow at T2 fluctuate in opposite phases, resulting in either independent or synchronous relationship between the instantaneous downstream and upstream bubble velocities depending on the operating conditions. Compared with two-phase flow, the modified capillary number and the ratio of the upstream velocity to the aqueous phase velocity were introduced to predict the bubble breakup time. The critical bubble breakup length and size laws of daughter bubbles/slugs were thereby proposed. These results provide an important guideline for designing microchannel structures for a precise manipulation of gas-liquid-liquid three-phase flow which finds potential applications among others in chemical synthesis.

Key words: microreactor, microfluidics, multiphase flow, bubble phenomena, bubble breakup

Introduction

Gas-liquid-liquid three-phase reactions are commonly encountered in various chemical

* Corresponding author. Tel.: +86-411-8437-9031, Fax.: +86-411-8469-1570

E-mail address: gwchen@dicp.ac.cn (G.W. Chen), superyao@dicp.ac.cn (C.Q. Yao)

syntheses, like hydrogenation[1-3], hydroformylation[4] and carbonylation[5]. These reactions usually involve complex mass transfer steps[6,7], including first the absorption of reactive gases (e.g., H_2, syngas or CO) into the organic substrate phase and then the transfer of dissolved gases to the aqueous phase where a (homogeneous) catalyst is usually contained. This feature causes the overall reaction performance to be likely hindered by mass transport limitation. Therefore, an effective dispersion of reactants and large interfacial area are required to intensify gas-liquid-liquid mass transfer thereof. However, conventional reactors (e.g., stirred tank reactors) can hardly fulfill these requirements, leading to low reaction efficiency. Besides, these reactors usually exhibit poor controllability over the phase dispersion (e.g., by the presence of a broad distribution of bubble/droplet sizes, channeling and dead zones), and hence low reproducibility and poor predictability of product quality.

Microreactor is an attractive reactor type for carrying out these gas-liquid-liquid reaction processes by enabling effective mass transfer[8-11] and precise process control[12-14]. Yap et al.[2,3] have shown that a series of hydrogenation reactions operated in a gas-liquid-liquid segmented flow (characterized by the alternate passage of bubbles and droplets in a continuous liquid carrier) yielded higher conversion and yield compared with its batch counterpart. Nevertheless, these reactions still remain mass transfer limited[3] due to the non-optimized dispersion of bubbles and droplets. Their microreactor design was simple (i.e., using capillary setups) and somehow arbitrary given a serious lack of common knowledge in the manipulation of three-phase flow in this field. In fact, their experiments already showed that shorter continuous phase segments improved mass transfer and reaction performance. Hence, it is inferred that by adjusting the dispersion of bubbles/droplets in a three-phase flow, mass transfer rate may be improved by several folds, as reported in two-phase flow systems[15-17]. This necessitates a comprehensive investigation into such topic for a successful application of three-phase reactions in microreactors. In addition, a precise control over gas-liquid-liquid flow regime in microreactors enables other important applications such as kinetics determination[1], nanomaterial synthesis[18-21], chemical screening[22] and extraction enhancement[8-10]. Overall, an in-depth understanding into the dispersion of bubbles/droplets in microreactors and the underlying mechanism is of great importance for obtaining the desired reaction/separation performance in these target applications.

Gas-liquid-liquid three-phase flow could be generated in several microreactor structures, such as microchannels with a cross-junction[8,23] or a double T-junction[1-3,9-12,24,25], and dual-coaxial microchannels[19,20]. The double T-junction configuration is the most common structure in use because of its assembly-oriented facility[1,9-11] (e.g., can be easily realized via a combination of capillary tubes and T-type connectors) and flexibility in multistep injection[26]. In a typical double T-junction configuration, bubbles are formed at the first T-junction and are usually subject to breakup at the second T-junction by impinging the second liquid phase[24-26], especially when large gas-liquid ratio is employed. This breakup (or bubble splitting) is of great importance as it dictates the size laws of the dispersed bubbles and droplets, as well as the flow characteristics therein. Currently, most literature on three-phase flow generation in microfluidic systems only involved short and non-breakup bubbles[12,23-25,27,28], indicating a knowledge gap concerning bubble splitting that is inevitable under conditions with large gas holdup. Wang et al.[24] proposed a model to predict the average bubble/droplet length by assuming that the phase interaction at the second T-junction would not influence hydrodynamics at the first T-junction. This assumption is well fulfilled when the velocity of the second liquid phase is much smaller than the bubble velocity from upstream, whereas much deviation occurs under other conditions[12,25]. In addition, their model could only predict the average length of bubbles/droplets instead of the separate lengths of daughter bubbles/droplets split at different stages, which greatly reduces the accuracy and application of such model. This suggests that a more in-depth investigation into the bubble breakup mechanism in a double T-junction microchannel is still necessary in order to fully understand the bubble/droplet generation and dispersion characteristics.

The existing numerous research on the breakup process of gas bubbles or liquid droplets in two-phase microchannel systems can shed light on the bubble breakup process in gas-liquid-liquid three-phase microflow. In two-phase microchannel systems, the breakup processes of bubbles/droplets arriving at a T-junction can be classified as the type ‘breakup with permanent obstruction’ in which bubbles/droplets totally obstruct the microchannel throughout the whole breakup process, and the type ‘breakup with tunnel’ in which a tunnel between bubbles/droplets and the wall opens[29]. These breakup types are present under a wide range of capillary numbers (Ca) depending on the bubble length. At relatively high Ca numbers (of a magnitude of 10^{-2}), Link

et al.[30] attributed the mechanism of 'breakup with tunnel' to the classical Rayleigh-Plateau instability and proposed a critical *Ca* number for determining the boundary between the breakup and non-breakup droplets. But at low and medium *Ca* numbers (e.g., with high surface tension values for the fluid system), Leshansky et al.[31,32] proposed that this breakup type was caused by the pressure in the lubrication film between the droplet and the channel wall. They derived a critical droplet breakup length that is proportional to $Ca^{-0.21}$ based on a 2-D lubrication analysis. As to the 'breakup with permanent obstruction', it usually occurs with relatively long droplets and low viscous continuous phase[29]. Also through a 2-D model, Leshansky et al.[33] showed that in the surface tension-dominated system, the breakup time was negatively associated with the flow rate and *Ca* number. However, this model failed to predict both the numerical and experimental results in 3-D systems[34-36]. Hoang et al.[34] ascribed this discrepancy to a three-dimensional capillary effect driven by the larger surface tension at the stagnation point. The above studies reveal that the interaction between phases has a significant effect on the breakup process, especially when surface tension plays an important role[37,38].

In gas-liquid-liquid microfluidic systems, the presence of a second liquid phase would certainly increase the effect of phase interaction on the bubble breakup. The underlying rupture mechanism might thus differ significantly from that in two-phase systems. Therefore, efforts need to be taken for a better design and operation of three-phase microfluidic systems[1-3,9-12,21-26,39,40]. This work concerns bubble breakup process under a gas-liquid-liquid flow in a microchannel with a double T-junction, aiming at improving the fundamental understanding thereof. Gas-oil segmented flow with slender bubbles was generated at the first T-junction, followed by bubble squeezing and splitting by the dispersed aqueous phase at the second T-junction. Types of the breakup regime, flow fluctuation, evolution of interfaces and breakup time were presented and discussed. Subsequently, the critical bubble breakup length and size laws of daughter bubbles/slugs thereof were proposed.

Experimental Section

Microchannel device and experimental setup

The gas-water-oil three-phase flow experiments were carried out in the microchannel device

(under horizontal orientation) shown in Fig. 1. The microchannel structure was fabricated on a transparent PMMA (polymethyl methacrylate) plate by precision milling technology (fabrication tolerance: 10 μm), covered by a second blind PMMA plate and sealed by bolted joints. All microchannels are 600 μm in width and 300 μm in depth and the serpentine main channel with half-circle connections is 44 cm long in total. The lengths of side channels 1, 2, 3 are 16, 40, 16 mm, respectively. The distance between the first and second T-junctions is 17 mm.

Oil and water were injected to inlet 1 and inlet 3 by syringe pumps (LSP02-1B, LongerPump, China), respectively. Gas was delivered from a cylinder to inlet 2 through a mass flow controller (SC200, Sevenstar, China) which was calibrated in advance. Thus, the gas-oil two-phase flow was formed at the first T-junction (abbreviated as T1) and the gas-water-oil three-phase flow at the second junction (abbreviated as T2). The experimental zone of interest is indicated by the blue dotted box in Fig. 1. The three-phase flow in the main channel was recorded by a high-speed CMOS camera (Phantom M310, Vision Research, USA, working at 500-1000 frames/s) supplemented by an optical microscope (SZX 16, Olympus, USA).

Figure 1. Schematic of the horizontally placed microchannel device with a double T-junction. The view section for camera snapshots is shown by the blue dotted box.

Experimental procedure

In the experiments, nitrogen, aqueous glycerol solutions and *n*-octane with 2.5 wt% Span 80 were chosen as the working fluids. N-octane added with surfactants has lower interfacial tension with the channel wall in comparison to the aqueous counterpart, thus the oil phase acted as the continuous phase. Physical properties of these fluids are listed in Table 1. Viscosities were measured with a viscometer (DV-II+Pro, Brookfield, USA). Interfacial tensions between gas phase/aqueous solutions and oil phase were measured by a tensiometer (DataPhysics OCA 15EC, Germany) using pendent drop method. Refractive indexes and densities were obtained from the literature[41]. As can be seen, refractive indexes of the investigated aqueous solutions and oil phase are very close. Therefore, 0.02 wt% of methyl orange was added into the aqueous solutions to make it easier to distinguish the different phases. Adding such a small amount of methyl orange

had little effect on the viscosity and interfacial tension according to our measurements. The experiments were carried out at room temperature (20±2 ^{o}C) and ambient pressure, the flow rate ranges of oil, gas and water phases being 0.10-0.30, 0.20-1.60 and 0.10-0.50 mL/min, respectively. Before recording the flow patterns, the system was running for at least 5 minutes to ensure the establishment of a stable flow.

Table 1. Physical properties of the used working fluids (20 ^{o}C, 0.1 MPa)

Results and Discussion

Breakup types and depression region evolution in T2

To facilitate the interpretation of our results, several important notations are defined here. The segments of the continuous phase are referred as 'plug' whereas the segments of dispersed aqueous droplets as 'slug'. Bubbles generated in T1 are called parent bubbles and denoted by PB, as shown in Fig. 2. If a parent bubble is cut off by the aqueous phase at T2, the first generated daughter bubble is called DB1 and the second DB2. The aqueous slugs formed within the duration are defined as S1 and S2, accordingly. During these breakup processes, the depression region refers to the water area between the bubble and the channel wall (Fig. 2). At the bottom of the depression region locates the stagnation point E, which is of the highest pressure and presets the droplet/bubble breakup point[30,37]. A is the obstruction point, where the parent bubble touches the channel wall as the obstruction initially occurs. The operating conditions are expressed in the form of 'oil flow rate-gas flow rate-aqueous flow rate (concentration of glycerol)'. For example, '0.10-0.35-0.20 (0 wt%)' indicates that the oil and gas flow rates are 0.10 and 0.35 mL/min, respectively, and the aqueous phase is deionized water of which the flow rate is 0.20 mL/min.

Figure 2. Important notations used in this paper. Aqueous phase is shown in orange, oil phase being the continuous carrier phase and gas bubbles being split at T2.

At T2, three bubble breakup types were observed as shown in Fig. 3: breakup with permanent obstruction (BPO), breakup with temporary obstruction (BTO) and non-breakup (NB), which are

similar to those observed in two-phase systems[29,37]. Their characteristics are summarized as follows:

(1) Type BPO (Fig. 3a) mainly happens in surface-tension dominated systems with low viscous aqueous phases (e.g., deionized water and 30 wt% glycerol solution). In this breakup type, the bubble obstructs the main channel and pinches off S1 immediately once the front bubble cap creeps out of the T2 zone, i.e., the obstruction point locates at the top-right corner of T2 (Fig. 3a, upper image). The depression region is always symmetric with respect to the centerline of T2, and the stagnation point locates at the centerline (Fig. 3a, middle image). When DB2 is about to leave T2, the aqueous phase is squeezed upwards due to its lower surface tension compared with the bubble (Fig. 3a, lower image). This may cause a large velocity fluctuation in the upstream flow.

(2) Type BTO (Fig. 3b) mainly occurs in systems with high viscous aqueous solutions (e.g., 50 wt% and 65 wt% glycerol solutions). The high viscosity of the aqueous phase makes slugs more difficult to be pinched off, resulting in the deformation of the front bubble cap. This also leads to the opening of a tunnel through which the aqueous phase flows downwards (Fig. 3b, upper image). With the parent bubble creeping, the tunnel narrows gradually and thins out finally to yield the aqueous slug S1 (Fig. 3b, middle image). We noticed that with more viscous aqueous phase, the obstruction point moves downwards and it takes longer time for the tunnel to thin out (see Fig. 3b, middle image, and Fig. 3c, upper image). With higher ratio of the upstream flow rate to the aqueous flow rate (i.e., Q_{up}/Q_W, where $Q_{up}= Q_O+Q_G$), the obstruction point also moves downwards as shown in Fig. 3c. After the tunnel disappears, an asymmetrical depression region with an off-center stagnation point is formed due to the high viscosity. Then the aqueous phase starts to squeeze and cut off the bubble neck (Fig. 3b, lower image).

(3) Type NB (Fig. 3d) happens in systems with relatively short parent bubbles or large upstream flow rates. In this type, the extra aqueous slugs may be sheared off by the continuous phase (i.e., free ruptured slug)[24,27]. Thus, more than one slug can be generated between two bubbles downstream.

Figure 3. Bubble breakup processes in the current microchannel device: (a) Type BPO, operating condition: 0.10-0.35-0.30 (0 wt%); (b) Type BTO, operating condition: 0.20-0.35-0.30

(50 wt%); (c) The effect of Q_{up}/Q_W on the obstruction point in BTO, operating conditions from top to bottom: 0.20-0.35-0.30 (65 wt%), 0.20-0.82-0.30 (65 wt%), 0.20-1.45-0.30 (65 wt%); (d) Type NB, operating condition: 0.20-0.16-0.30 (0 wt%).

For bubble breakup, the interface evolution provides rich information to explore the underlying mechanism. Fig. 4 presents an example of such evolution pattern based on the shape of the depression region in BPO. Shown in Fig. 4a is the characterization of the depression region, which is illustrated by the left expanded length L_l, the right expanded length L_r, the width ω and the location of stagnation point x_E. Fig. 4b depicts the evolution of these parameters from the parent bubble obstructing the channel to its breakup. As can be seen, the breakup process could be divided into three stages: the quick expansion stage, slow squeezing stage, and rapid collapse stage. The quick expansion stage starts at the moment when the parent bubble pinches off S1 and obstructs the channel totally (t=0). This obstruction induces quick augmentation of pressure in the aqueous phase, which further expands the depression region in both normal and tangential direction. During this stage, the stagnation point will be retracted back to the centerline (x_E =0) by surface tension whereas its original location is a little downstream due to the effect of the inertial force during S1 formation. The retraction is also the reason of the fast increase of L_l, which characterizes the quick expansion stage.

In the slow squeezing stage, the bubble deformation is mainly driven by the applied water flow while the effect of the upstream pressure is very small. The expansion of the depression region mainly takes place in the y-direction when $L_l \approx L_r > \omega$. At this time, the shape of the depression region resembles to the bubble/droplet breakup in two-phase flow[33,36]. However, when ω approaches L_l, the depression region keeps a semicircle shape ($L_l \approx L_r \approx \omega$) with three parameters increasing at the same pace. This shows that interfacial tensions start playing a dominant role over the upstream pressure and viscous force as $L_l \approx L_r \approx \omega$. It is in agreement with the phenomenon that the stagnation point E keeps staying at the y-axis.

When the depression region expands to a critical extent, it triggers the rapid collapse stage. At the critical time, the curvature at the stagnation point becomes the largest, which can easily lead to the spontaneous breakup of the bubble according to the surface-tension-driven mechanism

proposed by Hoang et al.[34] This mechanism suggests that the surface tension induces significant reverse flow to the stagnant point, which quickens the breakup. Besides, Wang et al.[35] suggested that when the bubble neck is thin enough, the circulation flow around the bubble neck would also aggravate the Raleigh-Plateau instability and the bubble breakup. The critical neck thickness in the case shown in Fig. 4 is found as δ_c/w=0.26 (i.e., =1-ω_c/w), which is in accordance with the literature[34-38]. Afterwards, the bubble neck shrinks and the water contracts from the two sides dramatically (indicated by the rapid decrease of L_l and L_r, and increase of ω) till the bubble ruptures (t=t_b).

Figure 4. (a) Typical sketch of bubble breakup process for BPO. J_{up} and J_W represent the superficial upstream bubble velocity (J_{up}=(Q_O+Q_G)/A_{CH}) and aqueous velocity (J_W=Q_W/A_{CH}), respectively. (b) Evolution of bubble breakup process. Three distinct stages are divided by blue dotted lines. The operating condition is 0.10-0.35-0.30 (0 wt%).

Flow fluctuation

The phenomenon that bubble neck obstructs the channel and ruptures periodically has been widely investigated in the bubble/droplet splitting[29,34,35,37,38] or formation processes[42,43]. These processes are always accompanied by the fluctuations of velocity and pressure. To gain a better understanding into the mechanism during bubble splitting in three-phase flow, we compared both the instantaneous bubble velocities in the upstream (U_{up}) and downstream (U_{down}) of T2. The bubble velocities were measured with Matlab (R2014b, The Mathworks, Inc., USA) by calculating the moving distance of bubble caps in a time step of 1-3 ms. We found that U_{down} could be either independent of or in synchronization with U_{up}. The possible reason could be related to hydrodynamics in the aqueous phase, so we estimated the instantaneous aqueous phase flow rate (Q_{EW}) according to the captured 2-D images. The estimation included the extraction of the 2-D area of unbroken slugs in each frame, and then multiplying them with channel height to obtain the instantaneous volume of water. The difference in the consecutive volume values divided by the time step was approximated as Q_{EW}, which turned out to fluctuate largely during the bubble splitting process.

Fig. 5 shows a typical case of U_{down} varying independently with U_{up}. The time t was scaled by bubble splitting period T. The measured U_{up} (U_{down}) and instantaneous Q_{EW} were scaled by the corresponding superficial values J_{up} (J_{down}) and Q_W, respectively. Clearly, the normalized downstream bubble velocity U_{down}/J_{down} keeps almost constant whereas the normalized upstream bubble velocity U_{up}/J_{up} varies periodically under the specified operating condition. Similar to two-phase systems, the decline in U_{up}/J_{up} occurs when the aqueous slug enters from the side channel to the main channel and leads to an increase in the flow resistance, whereas the rise in U_{up}/J_{up} occurs when the augmented upstream pressure starts to release and leads to fast shrinkage of the slug neck[44-47]. However, there are distinguishable characteristics for the three-phase system. As shown in Fig. 5, the rapid decrease in U_{up}/J_{up} from moment (3) to moment (5) originated from the increase in the flow resistance due to the slug tip squeezing the PB (moments (3)-(4)) and the slug blockage after the bubble ruptures (moments (4)-(5)). Interestingly, the decrease rate in U_{up}/J_{up} is larger after the bubble is pinched off. This suggests that the accumulation of flow resistance during the slug squeezing bubble is smaller than that during the slug blockage. It is reasonable as in the former case there is much larger space for the continuous phase flow around the bubble neck (especially when the diameter of the bubble neck is smaller than the channel depth, i.e., $\delta<h$) when bubble is not pinched off. The next decline of U_{up}/J_{up} from moments (6) to (7) is also due to the slug squeezing the DB2 and the slug blockage of the channel afterwards. As DB2 is not pinched off due to its relatively short length, neither dramatic shrinkage of bubble shape nor significant slope difference in U_{up}/J_{up} exists during the evolution.

From Fig. 5, it can also be seen that Q_{EW}/Q_W varies just in the opposite phase of U_{up}/J_{up}, showing that the periodic pressure accumulation/release in the upstream flow and aqueous flow are also in the opposite phases. For example, when the aqueous phase is firstly blocked by the PB (moments (2) to (3)), the slug tip cannot squeeze the PB due to the stronger gas-oil interfacial tension. The instantaneous flow rate of the aqueous phase decreases rapidly while its pressure accumulates fast[48]. As the augmented pressure becomes large enough to compete with interfacial tension, the bubble neck starts to shrink, leading to the pressure release in the aqueous phase (moments (3) to (5)). In the meanwhile, the flow resistance in the junction and the pressure of the upstream flow increase. In this way, the absolute flow fluctuations induced by the periodic

generation of slugs are offset, which results in a much stable flow in the downstream (stable U_{down}/J_{down}).

Figure 5. (a) Independent case showing the instantaneous evolutions of the upstream and downstream bubble velocities and the aqueous phase flow rate. (b) The corresponding flow images for moments (1)-(7) in (a). The operating condition is 0.10-0.35-0.30 (0 wt%); The dotted vertical line in (a) shows the bubble breakup moment; U/J equals $U_{up}A_{CH}/(Q_O+Q_G)$ for the upstream flow and $U_{down}A_{CH}/(Q_O+Q_G+Q_W)$ for the downstream flow.

For the synchronous case (Fig. 6), which occurs under the breakup type with temporary obstruction (BTO), the normalized upstream bubble velocity U_{up}/J_{up} also fluctuates periodically. But Q_{EW}/Q_W is much more smooth and steady compared with the independent case. In this case, the absolute fluctuation of Q_{EW} cannot offset that of U_{up}, leading to a synchronous variation between U_{down}/J_{down} and U_{up}/J_{up}. As can be seen, when U_{up}/J_{up} increases from moment (1) to moment (3) due to the pressure release of the upstream flow, Q_{EW}/Q_W only decreases significantly from moment (1) to moment (2). The generally stable aqueous flow from moment (2) to moment (3) results from the existence of an open tunnel which delays the pressure accumulation in the aqueous phase and further leads to the rebound of Q_{EW}/Q_W postponed to the moment (4), close to the bubble rupture. This is totally different from the independent case in which the rebound of Q_{EW}/Q_W occurs soon after T2 is blocked, as shown in Fig. 5. As a result, there are several durations in which Q_{EW}/Q_W varies very little and a significant fluctuation only occurs around the period during bubble breakup (moment (5)) and bubble cutting the slug (moment (1)). In addition, given the fact that Q_W herein is relatively small compared with the upstream flow rate Q_{up}, the aqueous phase flow fails to compensate the fluctuation of U_{up}, and thus U_{down}/J_{down} fluctuates in a synchronized pace with U_{up}/J_{up}.

Figure 6. (a) Synchronous case showing the instantaneous evolutions of the upstream and downstream bubble velocities and the aqueous phase flow rate. (b) The corresponding flow images for moments (1)-(8) in (a). The operating condition is 0.10-0.78-0.20 (50 wt%); The dotted

vertical line in (a) shows the bubble breakup moment; U/J equals $U_{up}A_{CH}/(Q_O+Q_G)$ for the upstream flow and $U_{down}A_{CH}/(Q_O+Q_G+Q_W)$ for the downstream flow.

Whether U_{down}/J_{down} varies synchronically with U_{up}/J_{up} depends on the viscosity of the aqueous phase μ_W and the upstream flow rate Q_{up}. As shown in Fig. 7, the increase in μ_W by an increase in glycerol concentration can lead to a transition from the independent variation to the synchronous variation. Although the magnitude of fluctuation in U_{up}/J_{up} is very large at relatively low μ_W (e.g., with 0 wt% glycerol in the aqueous phase), it is nearly completely offset by the aqueous flow, leading to a stable U_{down}/J_{down}. At relatively high μ_W, it usually induces the opening of a tunnel (i.e., breakup under BTO mode) which reduces the blockage of gas bubble. Therefore, the fluctuation in the aqueous flow rate tends to be smaller and cannot offset the fluctuation in U_{up}, leading to the synchronous variation. Meanwhile, the opening of the tunnel also reduces the squeezing force on the bubble. This results in the decreased magnitude of fluctuation in U_{up}/J_{up} when μ_W increases (i.e., at increasing glycerol concentration).

Figure 7. Effect of the viscosity of the aqueous phase (or glycerol concentration) on the fluctuation of the upstream and downstream bubble velocities. Q_O=0.10 mL/min, Q_G=0.35 mL/min, Q_W=0.30 mL/min. The text in the figure indicates the bubble breakup type and glycerol concentration in the aqueous phase. U/J equals $U_{up}A_{CH}/(Q_O+Q_G)$ for the upstream flow and $U_{down}A_{CH}/(Q_O+Q_G+Q_W)$ for the downstream flow.

Fig. 8 shows the effect of the upstream flow rate ($Q_{up}=Q_O+Q_G$) on the flow fluctuation. It can be seen that increasing Q_{up} has a similar effect to increasing μ_W, that is, a transition from the independent variation to the synchronous variation tends to occur upon increasing Q_{up}. Though higher Q_{up} results in both higher inertial force and viscous force exerted on the aqueous phase, the viscous force is not likely to dominate given the presence of the ultra-thin oil film (thickness below the optic resolution: ca. < 20 μm as measured from the flow images) in the depression region and the less significant shear stress at the gas-oil interface due to the low gaseous viscosity. By contrast, it is more likely the inertial force that adjusts the squeezing direction of the aqueous

phase and favors the tunnel opening, given somewhat large Reynolds number associated with the upstream flow (cf. Fig. 9 which will be discussed in detail hereafter). The absolute velocity fluctuation in U_{up} is observed to only increase slightly with the increase of Q_{up}. For example, the fluctuation ranges of U_{up} are within 0.022, 0.023, 0.028 m/s for Q_G=0.35, 0.82, 1.54 mL/min (or J_{up}=0.051, 0.094, 0.161 m/s) in Fig. 8, respectively. This results in an increased fluctuation in U_{down}/J_{down} (Fig. 8) due to the smoother Q_{EW}/Q_W caused by the tunnel opening especially facilitated at higher Q_{up} values (see Fig. 3c). Although the decrease in the normalized fluctuation magnitude in U_{up} (i.e., associated with U_{up}/J_{up}) upon increasing Q_{up} as shown in Fig. 8 is partly caused by the increased denominator (i.e., J_{up}), this does signify the important effect of the inertial force in lowering the flow fluctuation in the upstream. In other words, without the effect of the inertial force in facilitating the tunnel opening at higher Q_{up}, the evolution of the depression region in all cases shown in Fig. 8 should be under BPO mode. Then, at higher Q_{up}, the pressure accumulated in the upstream flow in this mode should be higher during the slug tip squeezing the PB (Fig. 5b, moments (3)-(4)) and the slug blockage after the bubble ruptures (Fig. 5b, moments (4)-(5)), which should result in a larger or at least the same magnitude of fluctuation in U_{up}/J_{up} when it releases (Fig. 5b, moments (5)-(6)).

Figure 8. Effect of the upstream flow rate on the fluctuation of the upstream and downstream bubble velocities. 30 wt% glycerol solution serves as the aqueous phase. Q_O=0.20 mL/min, Q_W=0.40 mL/min. The breakup types and Q_G are shown in the figure text. U/J equals $U_{up}A_{CH}/(Q_O+Q_G)$ for the upstream flow and $U_{down}A_{CH}/(Q_O+Q_G+Q_W)$ for the downstream flow.

From the analysis above, it is concluded that the velocity variation pattern is a result of the interaction among the phases at T2. Two main factors have been observed: the first one is the viscosity of the aqueous phase that influences the competition between the aqueous viscous force and interfacial tension; the other one is the upstream flow rate that influences the inertial force exerted on the aqueous phase. Therefore, Ca_W and Re_{up} are chosen to map the variation pattern of U_{up} and U_{down}. Ca_W is defined in Eq. (1), which represents the importance of the aqueous viscous force over the interfacial tension.

$$Ca_{\mathrm{W}} = \frac{\mu_{\mathrm{W}} Q_{\mathrm{W}}}{\gamma_{\mathrm{O\text{-}G}} A_{\mathrm{CH}}} \tag{1}$$

In the estimation of Ca_{W}, the oil-gas interfacial tension $\gamma_{\mathrm{O\text{-}G}}$ is employed because it is the oil phase that directly touches the gas bubble and determines the bubble neck shape. The aqueous viscosity is adopted since the oil film is so thin that its velocity gradient is likely to be almost constant, implying that the shear force exerted on the gas-oil interface might be roughly equal to that on the oil-water interface (i.e., as if there is a direct shear action of the aqueous phase on the gas bubble). Re_{up} is the Reynolds number of the upstream flow defined as

$$Re_{\mathrm{up}} = \frac{d_{\mathrm{h}} (Q_{\mathrm{O}} + Q_{\mathrm{G}}) \rho_{\mathrm{O}}}{\mu_{\mathrm{O}} A_{\mathrm{CH}}} \tag{2}$$

The obtained map is shown in Fig. 9, where five distinguished zones are identified as follows:

(a) Zone I: the interfacial tension dominated zone. In this zone ($Ca_{\mathrm{W}} < 0.009 - 0.00015 Re_{\mathrm{up}}$), the interfacial tension dominates over the aqueous viscous force and the upstream inertial force, and only the independent variation pattern is included.

(b) Zone II: the transition zone where the interfacial tension is comparable to the viscous force or the upstream inertial force; both independent and synchronous variation patterns are observed in this zone. The transition line is depicted as $Ca_{\mathrm{W}} = 0.009 - 0.00015 Re_{\mathrm{up}}$.

(c) Zone III: the aqueous viscous force dominated zone ($Ca_{\mathrm{W}} > 0.009$ and $Re_{\mathrm{up}} < 60$), which only includes synchronous variation pattern.

(d) Zone IV: the upstream inertial force dominated zone ($Ca_{\mathrm{W}} < 0.009$ and $Re_{\mathrm{up}} > 60$). In this zone, the inertial force dominates over the viscous force and interfacial tension, and only the synchronous variation pattern is included.

(e) Zone V: the synergistic zone of the aqueous viscous force and upstream inertial force ($Ca_{\mathrm{W}} > 0.009$ and $Re_{\mathrm{up}} > 60$). Since both forces facilitate the opening of tunnel, only the synchronous variation pattern is included.

It should be noted that the variation pattern is closely related to the breakup type, hence the map in Fig. 9 can be used to distinguish types BPO and BTO: Type BPO mainly locates at zone I, while types BTO at zones III, IV, and V.

Figure 9. Map of the bubble velocity variation pattern. The triangular box (II) shows the transition zone.

Bubble breakup time and size prediction

The critical bubble breakup length is an important parameter in the control of three-phase flow. For example, in order to achieve a quantitative dosing[26,40], the manipulation of a multistep synthesis process requires that the three-phase flow regime be kept in the non-breakup zone. In two-phase flow, the critical droplet breakup length was proposed either by capillary instability[30] or lubrication analysis[31]. In three-phase flow, whether a parent bubble is split or not at T2 is governed by the rule that the time for the parent bubble passing T2 should be larger than its breakup time[24]:

$$\frac{(L_{\mathrm{PB}} - w_{\mathrm{s}})}{J_{\mathrm{up}}} > t_{\mathrm{b}} \tag{3}$$

where w_s=w in the current microchannel. So the bubble breakup time needs to be derived first.

Leshansky et al.[33] developed a 2-D model to illustrate the droplet breakup with permanent obstruction in liquid-liquid two-phase flow in a microfluidic T-junction, as shown in Fig. 10. The model assumes that the shear force of the external flow (i.e., continuous flow in the case of Fig. 10) is always balanced by the interfacial tension at point B, which means that the depression region keeps a steady-state evolution[49]. Another assumption is that the depression region can be depicted as a circular arc with radius $R(t)$ and a small angle φ, thus L_r=Rsinφ~$R\varphi$ and ω=R(1-cosφ)~$^1/_2R\varphi^2$. For simplification, it is assumed that the continuous flow does not leak through the gap between the droplet and the channel wall. Thus, the increase rate of the area of the depression region (=R^2(φ–1/2sin2φ)~2$R^2\varphi^3$/3) equals to the mean inlet flow rate,

$$\frac{d}{dt}(\frac{2}{3}R^2\varphi^3) \approx J_{\mathrm{C}}w \tag{4}$$

If the continuous phase perfectly wets the channel wall, the balance between the interfacial tension and viscous force around the depression region edge B can be described by the Tanner's law[50], which suggests that φ^3 ~dL_r/dt·μ_C/γ. Then, the expansion rate of the depression region (dL_r/dt) reads

$$\frac{d}{dt}(R\varphi) \approx \frac{\alpha}{3Ca_C} J_C \varphi^3 \tag{5}$$

Where $Ca_C = \mu_C J_C/\gamma$. Solving Eq. (4) and Eq. (5) yields the evolution of L_r and ω as

$$\frac{L_r}{w} = 1.289\left(\frac{\alpha}{3Ca_C}\right)^{1/7}\left(\frac{J_C t}{w}\right)^{4/7} \tag{6}$$

$$\frac{\omega}{w} = 0.582\left(\frac{\alpha}{3Ca_C}\right)^{-1/7}\left(\frac{J_C t}{w}\right)^{3/7} \tag{7}$$

where α was approximated as 0.25 by fitting to 2-D numerical simulation results[33]. Then the droplet breakup time is calculated as the time needed for the depression region width to be equal to the channel width (ω=w):

$$t_b = 3.54\frac{w}{J_C}\left(\frac{\alpha}{3Ca_C}\right)^{1/3} \tag{8}$$

This correlation indicates that the droplet breakup time is negatively dependent on the capillary number of the carrier liquid (Ca_C).

Figure 10. Schematic of the depression region in a typical 'obstructed' breakup regime in two-phase flow in a microfluidic T-junction according to the model of Leshansky et al.[33] The side and main channels have the same width (i.e., w_s=w).

The above model is firstly applied to describe the bubble breakup under BPO mode in gas-liquid-liquid three-phase system in the current microchannel. It is expected to be approximately valid because all the aqueous phase squeezes the bubble without leakage due to the existence of the oil-water interface. In addition, the inertial of the upstream flow is very small compared with the interfacial tension in BPO, as shown previously in this paper (e.g., see zone I in Fig. 9). Therefore, the main deviation from this model is that the viscous force of the aqueous phase has to overcome the oil-gas interfacial tension as explained above (Eq. (1)). This leads to a revision of the Tanner's law[50] as $\varphi^3 \sim dL_r/dt \cdot \mu_W/\gamma_{O\text{-}G}$. The usage of the aqueous viscosity is because that aqueous phase fills the depression region. Accordingly, the modified 2-D model of Leshansky et al.[33] is obtained as

$$t_{b,L} = 3.54\frac{w}{J_W}\left(\frac{0.25}{3Ca_W}\right)^{1/3} = 1.54\frac{w}{J_W}Ca_W^{-1/3} \quad (9)$$

We compared the prediction of Eq. (9) with the experimental results and found that the prediction is about 10 times larger. There are two important reasons that result in this large discrepancy. Firstly, the model developed from 2-D analysis deviates much from the real 3-D conditions. The prediction of the model of Leshansky et al.[33] has also been shown to be 4-6 times higher than the simulated and measured bubble/droplet breakup time in two-phase flows[34,36]. Hoang et al.[34] found that the 2-D model can well predict the depression region in their 3-D simulation only before the bubble neck reaches the critical thickness (δ_c). They proposed that the interfacial tension induced circulation near the neck could accelerate the breakup, which is however not considered in the 2-D model. The second reason is that the spread of the dispersed aqueous phase in *x*-axis in three-phase flow is more difficult than that of the perfect wetting continuous phase in two-phase flow, which causes a much stronger squeezing on the gas bubble in *y*-axis (e.g., see Fig. 4(a)). This is reasonable since: (1) the squeezing phase in three-phase flow is the dispersed phase which is restricted by the oil-water interface; (2) the aqueous phase in three-phase flow cannot well wet the current microchannel wall made of PMMA preceding its expansion (due to the poor aqueous wettability, e.g., the deionized water-solid contact angle in the continuous oil phase is 135°) while the perfect wetting continuous phase does in two-phase flow. This also explains why the prediction of the 2-D model shows a larger divergence in three-phase flow than that in two-phase flow cases. Fig. 11 shows the comparison between the 2-D model and our experimental results of L_r and ω. As can be seen, the experimental L_r is much smaller, whereas ω is much larger than the model prediction at the later stage of the squeezing, suggesting that the spread of the aqueous phase in *x*-axis is largely confined.

Figure 11. Comparison of the depression region predicted by the model of Leshansky et al.[33] (i.e., Eqs. (6)-(7) in which Ca_C and J_C are replaced with Ca_W and J_W, respectively) and our experimental results. The solid lines are the experimental results and the dashed lines are obtained from the model.

Accordingly, a semi-empirical correlation similar to Eq. (9) is obtained for the breakup time under BPO mode through a regression of the experimental data:

$$t_{\mathrm{b,P}} = 0.165 \frac{w}{J_{\mathrm{W}}} Ca_{\mathrm{W}}^{-1/3} \tag{10}$$

$$t_{\mathrm{b,P}}^{*} = 0.165 \frac{J_{\mathrm{up}}}{J_{\mathrm{W}}} Ca_{\mathrm{W}}^{-1/3} \tag{11}$$

where $t_{\mathrm{b,P}}^{*}$ is the dimensionless breakup time scaled by w/J_{up} in BPO mode. The range of the operating conditions is $0.0004 < Ca_{\mathrm{W}} < 0.005$ and $0 < Re_{\mathrm{up}} < 60$. And the same exponent associated with Ca_{W} (i.e., -1/3 in Eq. (11)) is used because it is thought that the model of Leshansky et al.[33] is still approximately applicable to three-phase system, given many similarities in physical flow situation (or more precisely, in the governing equations of the interface evolution). Besides, a smaller coefficient (i.e., 0.165 here vs. 1.54 in Eq. (9)) is obtained by adjusting the value of α (cf. Eq. (8)) from 0.25 to 3.04×10^{-4}, which is acceptable because: (1) α is a fitting value resulting from sample data (i.e., either 2-D numerical simulation results[33] or 3-D experimental results); (2) α fitted by 3-D experimental results tends to be much smaller than that by 2-D numerical simulation results[33] due to the huge influence of the rapid collapse stage and much confined aqueous x-axial expansion on breakup time, as we have discussed previously (Fig. 11).

As to the bubble breakup under BTO mode, the upstream flow plays an important role as previously mentioned (e.g., see Fig. 9). Therefore, compared with Eq. (11), an additional modification over $J_{\mathrm{up}}/J_{\mathrm{W}}$ needs to be made here to depict the competition between the inertial force from the upstream flow and the squeezing from the aqueous phase. Then, a correlation for the breakup time in BTO mode is proposed as

$$t_{\mathrm{b,T}}^{*} = 1.926 \left(\frac{J_{\mathrm{up}}}{J_{\mathrm{W}}}\right)^{0.766} Ca_{\mathrm{W}}^{0.029} \tag{12}$$

where $t_{\mathrm{b,T}}^{*}$ is the dimensionless breakup time scaled by w/J_{up} in BTO mode. The range of the operating conditions is $0.005 < Ca_{\mathrm{W}} < 0.022$ and $0 < Re_{\mathrm{up}} < 100$. The positive exponent with Ca_{W} in this correlation is due to the existence of an open tunnel between the bubble and the channel wall. In BTO mode, the bubble breakup time consists of two parts: the tunnel time during which the aqueous phase flow through the tunnel, and subsequently the obstruction time during which the channel is obstructed by the bubble and the aqueous phase squeezes the bubble. The tunnel

time is positively correlated to Ca_W (e.g., the tunnel width is shown to follow a law of $Ca_W^{0.4}$ in two-phase systems[29,31]) while the obstruction time is negatively correlated to Ca_W as indicated by Eq. (10). Therefore, it is reasonable that the tunnel time dominates over the obstruction time, resulting in a positive exponent with Ca_W. It can be seen that both the predictions of Eqs. (11) and (12) agree well with the experimental results (Fig. 12).

Figure 12. Comparison of the predicted dimensionless bubble breakup time vs. the experimental results. Eqs. (11) and (12) are used as the models for BPO and BTO modes, respectively.

As the bubble breakup time is obtained, the critical bubble length and the size laws of daughter bubbles/slugs can be derived. According to Eq. (3), if the length of a PB is larger than its moving distance during the breakup time, the PB will rupture. A margin length equal to the side channel width (w_s=w in our experimental conditions) was introduced in Eq. (3) since the squeezing starts when the bubble completely covers the side channel, as indicated by the simplified process shown in Fig. 13 (i.e., at t = 0). However, we suggest this margin length to be w+w_s since the blockage of the side channel is still needed when the bubble ruptures (i.e., L_{DB2}≥1/2(w_s+w)=w in the current experiments). Thus, the critical bubble breakup length can be written as

$$\frac{L_c}{w} = t_b^* + \frac{w_s + w}{w} = t_b^* + 2 \tag{13}$$

Figure 13. Simplified bubble breakup process for BPO mode (w_s=w in the current microchannel).

According to the simplified model for the breakup process proposed in Fig. 13, the lengths of DB1 and DB2 are then estimated as:

$$\frac{L_{DB1}}{w} = t_b^* + 1 \tag{14}$$

$$\frac{L_{DB2}}{w} = \frac{L_{PB}}{w} - t_b^* - 1 \tag{15}$$

It should be noted that the above analysis only considers the situation when a PB splits into two

daughter bubbles. If a PB splits into more than two bubbles, DB2 can be treated as a new PB and the analysis is also applicable. In our experimental conditions, the splitting of DB2 only happens rarely in BTO mode with extremely long bubbles and very large aqueous flow rates. Fig. 14 shows a comparison between the measured length of PB and the critical bubble length predicted by Eq. (13) in which t_b^* was calculated by Eqs. (11) and (12) for BPO and BTO modes, respectively. As can be seen, a good prediction over whether the bubble breaks up or not is obtained in both modes (i.e., bubble is split at $L_{PB} \geq L_c$).

Figure 14. Comparison between the measured PB lengths and the predicted critical ones (with Eqs. (11)-(13)). The solid and open symbols stand for data under BPO and BTO modes, respectively. The solid line represents the parity line.

When a parent bubble breaks into two daughter bubbles under BPO mode, S2 is generated between them. The total generation time includes the bubble breakup time (t_b) and the time for DB2 to cut S2 off (t_c). The second time duration allows DB2 to move a distance of $w+w_s$, as shown in Fig. 13 ($t_c=(w+w_s)/J_{up}$; $w_s=w$ in the present experiments). Then, the length of S2 is derived as

$$\frac{L_{S2}}{w} = \frac{J_W\left(t_b + t_c\right)}{w} = (t_b^* + \frac{w + w_s}{w})\frac{J_W}{J_{up}} = (t_b^* + 2)\frac{J_W}{J_{up}} \tag{16}$$

Besides, the frequency of the parent bubble equals to that of S1 and S2. If we neglect the slip velocity between bubbles and the aqueous slugs, the following equation holds approximately:

$$\frac{L_{PB}}{L_{S1} + L_{S2}} \approx \frac{J_G}{J_W} \tag{17}$$

Therefore, the length of S1 could be estimated from:

$$\frac{L_{S1}}{w} \approx \frac{L_{PB}}{w}\frac{J_W}{J_G} - \frac{L_{S2}}{w} \tag{18}$$

As can be seen in Fig. 15a, the proposed model (i.e., Eqs. (13)-(16) and (18)) provides a good prediction over the lengths of daughter bubbles and slugs measured in our experiments under mode BPO. The small deviations are mainly caused by the flow fluctuations mentioned above. For

example, during the generation process of DB1 (Fig. 5, moments (1)-(4)), the average U_{up} is higher than the corresponding superficial value (i.e., J_{up}) that is utilized in Eq. (14) for the calculation of t_b^*, which results in the underestimation of L_{DB1} shown in Fig. 15a as well as an overestimation of L_{DB2}. Thus, it is expected that the smoother the flow fluctuation, the higher the prediction accuracy of this model. Interestingly, this proposed model also works well under BTO mode (Figs. 14 and 15b), though the simplified breakup process shown in Fig. 13 differs greatly from the real evolution process in BTO. This indicates that a good estimation of the bubble breakup time (e.g., Eq. (12)) is essential in the size law prediction. Since the detailed breakup mechanism under BTO mode is not very clear yet, more dedicated studies are still needed in this direction. It should be noted that this model is derived for the present microchannel with a double T-junction characterized by equal widths of side and main channels, thus its applicability in other configurations (e.g., with different side channel widths) still needs to be examined.

Figure 15. Comparison between the predicted daughter bubble/slug lengths and the experimental results: (a) type BPO; (b) type BTO. L_{DB1}, L_{DB2}, L_{S2}, L_{S1} are predicted by Eqs. (14)-(16) and (18), respectively.

In order to further confirm the validity of our model, the measured L_{S2} values under mode BPO was compared in Fig. 16 with the literature data (i.e., those obtained by Wang et al.[24] during three-phase flow in a similar microchannel geometry; the original data in Fig. 8 of their work were reprocessed to estimate the corresponding L_{S2} values as a function of J_W). As can be seen, the measured L_{S2} in our experiments follows a linear relationship with J_W for a given Q_{up} (or J_{up}) value, as indicated from Eq. (19) (which is derived from Eqs. (11) and (16)):

$$\frac{L_{S2}}{w}=\left(t_{b,P}^{*}+\frac{w+w_s}{w}\right)\frac{J_W}{J_{up}}=0.165Ca_W^{-1/3}+\left(1+\frac{w_s}{w}\right)\frac{J_W}{J_{up}} \tag{19}$$

Furthermore, Eq. (19) also correctly reveals the decreased L_{S2} and linear slope with the increase of Q_{up} (or J_{up}), as experimentally observed (Fig. 16). However, regarding the literature data[24], although a linear relationship seems to exist between L_{S2} and J_W, the influence of Q_{up} (or J_{up}) on L_{S2} cannot be revealed because the exact Q_{up} (or J_{up}) value for a given J_W is not available. It can

also be seen in this figure that L_{S2}/w values from the literature[24] (under the condition that 0.23 ml/min $<Q_{up}=Q_G+Q_O<$ 0.64 ml/min) is lower than ours (under the condition that 0.37 ml/min $<Q_{up}$ < 0.68 ml/min). This discrepancy, albeit somewhat comparable ranges of Q_{up} or J_{up} in both cases, might arise from the different microchannel configuration in use (w_s/w=0.5 in the literature[24] while w_s/w=1 in our work). In addition, the roughly equal y-intercepts for all the straight lines could be anticipated from Eq. (19) of which the first term in the right side, i.e., $0.165Ca_W^{1/3}$, is roughly close to each other under the literature conditions (ca. in a range of 0.6-2.3) and ours (ca. in a range of 1.0-2.2). Therefore, the model introduced in the present work is considered to be accurate, robust and physically reasonable.

Figure 16. Comparison between our experimental results on L_{S2}/w (closed symbols) and those of the literature[24] (+). Operating conditions in our experiments: the aqueous phase is deionized water, Q_W = 0.2-0.8 mL/min, Q_G = 0.28 mL/min, and Q_{up} is adjusted by the oil flow rate; Operating conditions in the literature[24]: Q_G = 0.182-0.512 mL/min, Q_O = 0.050-0.125 mL/min in the air-PEG aqueous solution-*n*-octane (with 2 wt% Span-80) system.

Conclusions

Gas-liquid-liquid three-phase flow is frequently encountered in various chemical syntheses with aqueous-organic catalysis (e.g., hydrogenation, hydroformylation and carbonylation). The performance of such processes, when carried out in conventional reactors, tends to be hindered by mass transfer limitation due to the presence of three phases rendering difficulties in a precise control over flow pattern and interfacial area. In this respect, microreactors provide unique potential in the intensification of these chemical processes by offering effective dispersion of reactants and large interfacial area in microchannels.

This paper presents an experimental investigation into the bubble breakup process in a gas-aqueous liquid-oil three-phase flow generated in a microchannel with a double T-junction. The bubble breakup at the second T-junction is found as a result of the competition between the squeezing of the dispersed aqueous phase and the inertial force of the upstream gas-oil flow. Therefore, different breakup types can be mapped based on the capillary number of the aqueous phase (Ca_W) and Reynolds number of the upstream flow (Re_{up}). When interfacial tensions are

dominant (i.e., at low Ca_W and Re_{up}), the bubble breakup type is 'breakup with permanent obstruction' (BPO). Due to blockage of the gas bubbles, the instantaneous upstream bubble velocity and aqueous flow rate fluctuate in the opposite phases. These fluctuations are perfectly compensated in BPO mode, leading to an almost invariable bubble velocity in the downstream. When the viscous or inertial force plays an important role (i.e., at high Ca_W or Re_{up}), the 'breakup with temporary obstruction' (BTO) occurs and is characterized by an open tunnel for the aqueous phase to flow through. This leads to a partial compensation of the flow fluctuations in the upstream bubble and the aqueous phase, and therefore a synchronous variation pattern in the bubble velocity develops between the downstream and upstream.

In this work, a 2-D model of Leshansky et al.[33] describing the evolution of the squeezed droplet interface in two-phase microflows is applied to the present three-phase system after some modifications. According to the distinct three-phase flow characteristics therein, Ca_W and the ratio of the upstream to aqueous phase flow rate are introduced to modify the model, based on which two semi-empirical correlations (Eqs. (11) and (12)) are proposed to predict the bubble breakup time for both BPO and BTO modes. Moreover, the critical bubble length and size laws for the generated daughter bubbles/droplets are obtained (Eqs. (13)-(16) and (18)). The proposed length model well predicts the experimental results and is considered to be physically reasonable. The findings in this work can serve as an important guideline for the manipulation of flow regime/dispersion of gas-liquid-liquid flow in microreactors, which finds potential applications among others in chemical synthesis.

Acknowledgements

We acknowledge gratefully the financial support for this work from National Natural Science Foundation of China (Nos. 21676263, 91634204 and U1662124).

Notation

A_{CH} cross-sectional area of microchannel [$A_{CH}=wh$], m^2

d_h hydrodraulic diameter of main channel, m

h height of microchannel, m

J_C superficial velocity of the continuous phase [$J_C=Q_C/A_{CH}$], m/s

J_{down} superficial velocity of the downstream bubble [$J_{down}=(Q_O+Q_G+Q_W)/A_{CH}$], m/s

J_{up} superficial velocity of the upstream bubble [$J_{up}=(Q_O+Q_G)/A_{CH}$], m/s

J_W superficial velocity of the aqueous phase [$J_W=Q_W/A_{CH}$], m/s

L_c critical bubble breakup length, m

L_{DB1} length of the first daughter bubble, m

L_{DB2} length of the second daughter bubble, m

L_l left expanded length of the depression region, m

L_{PB} length of the parent bubble, m

L_r right expanded length of the depression region, m

L_{S1} length of the first aqueous slug, m

L_{S2} length of the second aqueous slug, m

Q_{down} preset downstream flow rate [$Q_{down}=Q_O+Q_G+Q_W$], m^3/s

Q_{EW} instantaneous aqueous flow rate, m^3/s

Q_G preset gas flow rate, m^3/s

Q_O preset oil flow rate, m^3/s

Q_{up} preset upstream flow rate [$Q_{up}=Q_O+Q_G$], m^3/s

Q_W preset aqueous flow rate, m^3/s

T bubble splitting period, s

t_b bubble breakup time measured from experiments, s

$t_{b,L}$ bubble breakup time estimated by the model of Leshansky et al.[33], s

$t_{b,P}$ predicted bubble breakup time for BPO mode, s

t_c time that DB2 needs to cut S2 off, s

U_{down} instantaneous downstream bubble velocity, m/s

U_{up} instantaneous upstream bubble velocity, m/s

w width of main microchannel, m

w_s width of side microchannel, m

Greek letters

$\gamma_{O\text{-}G}$ interfacial tension between oil and gas, N/m

$\gamma_{O\text{-}W}$ interfacial tension between oil and the aqueous phase, N/m

δ neck thickness of bubble, m

μ_W viscosity of the aqueous phase, Pa·s

μ_O viscosity of the oil phase, Pa·s

ρ_O density of the oil phase, kg/m^3

φ angle of the depression region edge

ω width of the depression region, m

Dimensionless groups

Ca_C capillary number of the continuous phase in two-phase flow [$Ca_C=\mu_C J_C/\gamma$]

Ca_W capillary number of the aqueous phase in three-phase flow [$Ca_W=\mu_W J_W/\gamma_{O\text{-}G}$]

Re_{up} Reynolds number of the upstream gas-oil flow [$Re_{up}=d_h Q_{up}\rho_O/\mu_O A_{CH}$]

t_b^* dimensionless bubble breakup time

$t_{b,P}^*$ dimensionless bubble breakup time for BPO mode

$t_{b,T}^*$ dimensionless bubble breakup time for BTO mode

Literature Cited

1. Önal Y, Lucas M, Claus P. Application of a capillary microreactor for selective hydrogenation of α,β-unsaturated aldehydes in aqueous multiphase catalysis. *Chem. Eng. Technol.* 2005;28(9):972-978.
2. Yap SK, Yuan Y, Zheng L, Wong WK, Yan N, Khan SA. Triphasic segmented flow millireactors for rapid nanoparticle-catalyzed gas-liquid reactions - hydrodynamic studies and reactor modeling. *J. Flow Chem.* 2014;4(4):200-205.
3. Yap SK, Yuan Y, Zheng L, Wong WK, Yan N, Khan SA. Rapid nanoparticle-catalyzed hydrogenations in triphasic millireactors with facile catalyst recovery. *Green Chem.* 2014;16(11):4654-4658.
4. Purwanto P, Delmas H. Gas-liquid-liquid reaction engineering: hydroformylation of 1-octene using a water soluble rhodium complex catalyst. *Catal. Today.* 1995;24(1-2):135-140.
5. Didgikar MR, Joshi SS, Gupte SP, Diwakar MM, Deshpande RM, Chaudhari RV. Oxidative carbonylation of amine using water-soluble palladium catalysts in biphasic media. *J. Mol. Catal. A: Chem.* 2011;334(1-2):20-28.

6. Chaudhari RV, Bhattacharya A, Bhanage BM. Catalysis with soluble complexes in gas-liquid-liquid systems. *Catal. Today.* 1995;24(1-2):123-133.
7. Dumont E, Delmas H. Mass transfer enhancement of gas absorption in oil-in-water systems: a review. *Chem Eng Processing: Process Intensification.* 2003;42(6):419-438.
8. Su YH, Chen GW, Zhao YC, Yuan Q. Intensification of liquid-liquid two-phase mass transfer by gas agitation in a microchannel. *AIChE J.* 2009;55(8):1948-1958.
9. Aoki N, Ando R, Mae K. Gas-liquid-liquid slug flow for improving liquid-liquid extraction in miniaturized channels. *Ind. Eng. Chem. Res.* 2011;50(8):4672-4677.
10. Assmann N, von Rohr PR. Extraction in microreactors: Intensification by adding an inert gas phase. *Chem. Eng. Processing: Process Intensification.* 2011;50(8):822-827.
11. Abolhasani M, Bruno NC, Jensen KF. Oscillatory three-phase flow reactor for studies of bi-phasic catalytic reactions. *Chem. Commun.* 2015;51(43):8916-8919.
12. Rajesh VM, Buwa VV. Experimental characterization of gas-liquid-liquid flows in T-junction microchannels. *Chem. Eng. J.* 2012;207-208:832-844.
13. Wan J, Stone HA. Microfluidic generation of a high volume fraction of bubbles in droplets. *Soft Matter.* 2010;6(19):4677.
14. Hashimoto M, Garstecki P, Whitesides GM. Synthesis of composite emulsions and complex foams with the use of microfluidic flow-focusing devices. *Small.* 2007;3(10):1792-1802.
15. Su YH, Zhao YC, Chen GW, Yuan Q. Liquid-liquid two-phase flow and mass transfer characteristics in packed microchannels. *Chem. Eng. Sci.* 2010;65(13):3947-3956.
16. Zhao YC, Chen GW, Yuan Q. Liquid-liquid two-phase mass transfer in the T-junction microchannels. *AIChE J*. 2007; 53(12):3042-3053.
17. Yue J, Chen GW, Yuan Q, Luo LA, Gonthier Y. Hydrodynamics and mass transfer characteristics in gas-liquid flow through a rectangular microchannel, *Chem. Eng. Sci*. 2007;62(7):2096-2108.
18. Lee M, Lee EY, Lee D, Park BJ. Stabilization and fabrication of microbubbles: applications for medical purposes and functional materials. *Soft Matter.* 2015;11(11):2067-2079.
19. Abbaspourrad A, Duncanson WJ, Lebedeva N, Kim SH, Zhushma AP, Datta SS, Dayton PA, Sheiko SS, Rubinstein M, Weitz DA. Microfluidic fabrication of stable gas-filled microcapsules for acoustic contrast enhancement. *Langmuir.* 2013;29(40):12352-12357.
20. Duncanson WJ, Abbaspourrad A, Shum HC, Kim SH, Adams LL, Weitz DA. Monodisperse

gas-filled microparticles from reactions in double emulsions. *Langmuir.* 2012;28(17):6742-6745.

21. Duraiswamy S, Khan SA. Plasmonic nanoshell synthesis in microfluidic composite foams. *Nano Lett.* 2010;10(9):3757-3763.
22. Zheng B, Ismagilov RF. A microfluidic approach for screening submicroliter volumes against multiple reagents by using preformed arrays of nanoliter plugs in a three-phase liquid/liquid/gas flow. *Angew Chem-Int Edit.* 2005;44(17):2520-2523.
23. Yue J, Rebrov EV, Schouten JC. Gas-liquid-liquid three-phase flow pattern and pressure drop in a microfluidic chip: similarities with gas-liquid/liquid-liquid flows. *Lab Chip.* 2014;14(9):1632-1649.
24. Wang K, Qin K, Lu YC, Luo GS, Wang T. Gas/liquid/liquid three-phase flow patterns and bubble/droplet size laws in a double T-junction microchannel. *AIChE J.* 2015;61(5):1722-1734.
25. Yao CQ, Liu YY, Zhao SN, Dong ZY, Chen GW. Bubble/droplet formation and mass transfer during gas-liquid-liquid segmented flow with soluble gas in a microchannel. *AIChE J.* 2016. DOI:10.1002/aic.15536.
26. Nightingale AM, Phillips TW, Bannock JH, de Mello JC. Controlled multistep synthesis in a three-phase droplet reactor. *Nature Comm.* 2014;5:3777.
27. Wang K, Lu YC, Tan J, Yang BD, Luo GS. Generating gas/liquid/liquid three-phase microdispersed systems in double T-junctions microfluidic device. *Microfluid. Nanofluidics.* 2009;8(6):813-821.
28. Ładosz A, Rigger E, von Rohr PR. Pressure drop of three-phase liquid–liquid–gas slug flow in round microchannels. *Microfluid. Nanofluidics.* 2016;20(3):49.
29. Jullien MC, Tsang Mui Ching MJ, Cohen C, Menetrier L, Tabeling P. Droplet breakup in microfluidic T-junctions at small capillary numbers. *Phys. Fluids* . 2009;21(7):072001.
30. Link DR, Anna SL, Weitz DA, Stone HA. Geometrically mediated breakup of drops in microfluidic devices. *Phys. Rev. Lett.* 2004;92(5):054503.
31. Leshansky AM, Pismen LM. Breakup of drops in a microfluidic T junction. *Phys. Fluids* . 2009;21(2):023303.
32. Afkhami S, Leshansky AM, Renardy Y. Numerical investigation of elongated drops in a microfluidic T-junction. *Phys. Fluids* . 2011;23(2):022002.
33. Leshansky AM, Afkhami S, Jullien MC, Tabeling P. Obstructed breakup of slender drops in a

microfluidic T junction. *Phys. Rev. Lett.* 2012;108(26):264502.

34. Hoang DA, Portela LM, Kleijn CR, Kreutzer MT, van Steijn V. Dynamics of droplet breakup in a T-junction. *J. Fluid. Mech.* 2013;717:R4.
35. Wang XD, Zhu CY, Fu TT, Ma YG. Bubble breakup with permanent obstruction in an asymmetric microfluidic T-junction. *AIChE J.* 2015;61(3):1081-1091.
36. Lu YT, Fu TT, Zhu CY, Ma YG, Li HZ. Dynamics of bubble breakup at a T junction. *Phys. Rev. E.* 2016;93(2):022802.
37. Fu TT, Ma YG, Funfschilling D, Li HZ. Dynamics of bubble breakup in a microfluidic T-junction divergence. *Chem. Eng. Sci.* 2011;66(18):4184-4195.
38. Wang XD, Zhu CY, Wu YN, Fu TT, Ma YG. Dynamics of bubble breakup with partly obstruction in a microfluidic T-junction. *Chem. Eng. Sci.* 2015;132:128-138.
39. Tan J, Dong C, Lu YC, Xu JH, Luo GS. Coupling process of oxidation and extraction in a gas-liquid-liquid microdispersion system for H_2O_2 synthesis. *Ind. Eng. Chem. Res.* 2012;51(4):1834-1845.
40. Li L, Boedicker JQ, Ismagilov RF. Using a multijunction microfluidic device to inject substrate into an array of preformed plugs without cross-contamination: comparing theory and experiments. *Anal Chem.* 2007;79(7):2756-2761.
41. Takamura K, Fischer H, Morrow NR. Physical properties of aqueous glycerol solutions. *J. Petro. Sci. Eng.* 2012;98-99:50-60.
42. van Steijn V, Kleijn CR, Kreutzer MT. Flows around confined bubbles and their importance in triggering pinch-off. *Phys. Rev. Lett.* 2009;103(21):214501.
43. Glawdel T, Elbuken C, Ren CL. Droplet formation in microfluidic T-junction generators operating in the transitional regime. I. Experimental observations. *Phys. Rev. E.* 2012;85(1):016322.
44. De Menech M, Garstecki P, Jousse F, Stone HA. Transition from squeezing to dripping in a microfluidic T-shaped junction. *J. Fluid. Mech*. 2008;595:141-161..
45. Li XB, Li FC, Yang JC, Kinoshita H, Oishi M, Oshima M. Study on the mechanism of droplet formation in T-junction microchannel. *Chem. Eng. Sci.* 2012;69(1):340-351.
46. Yan Y, Guo D, Wen SZ. Numerical simulation of junction point pressure during droplet formation in a microfluidic T-junction. *Chem. Eng. Sci.* 2012;84:591-601.
47. Yao CQ, Dong ZY, Zhao YC, Chen GW. The effect of system pressure on gas-liquid slug flow in a

microchannel. *AIChE J.* 2014;60(3):1132-1142.

48. Liu XD, Zhang CB, Yu W, Deng ZL, Chen YP. Bubble breakup in a microfluidic T-junction. *Sci. Bull.* 2016;61(10):811-824.
49. Navot Y. Critical behavior of drop breakup in axisymmetric viscous flow. *Phys. Fluids.* 1999;11(5):990.
50. Tanner LH. The spreading of silicone oil drops on horizontal surfaces. *J. Phys. D: Appl. Phys.* 1979;12(9):1473-1484.
51. Garstecki P, Fuerstman MJ, Stone HA, Whitesides GM. Formation of droplets and bubbles in a microfluidic T-junction-scaling and mechanism of break-up. *Lab Chip.* 2006;6(3):437-446.

Table list

Table 1. Physical properties of the used working fluids (20 ^{o}C, 0.1 MPa)

Phase	Fluid	Refractive index n	Viscosity μ [mPa·s]	Density ρ [kg/m^3]	Interfacial tension with oil γ [mN/m]
Oil	*n*-octane with 2.5 wt% Span 80	1.397	0.565	702	–
Gas	Nitrogen	1.000	0.018	1.271	21.94
Aqueous	Deionized water	1.333	1.002	1000	4.77
	30 wt % glycerol	1.375	2.29	1078	4.94
	50 wt % glycerol	1.404	5.28	1131	4.40
	65 wt % glycerol	1.425	12.82	1171	4.69

Figure lists

Figure 1. Schematic of the horizontally placed microchannel device with a double T-junction. The view section for camera snapshots is shown by the blue dotted box.

Figure 2. Important notations used in this paper. Aqueous phase is shown in orange, oil phase being the continuous carrier phase and gas bubbles being split at T2.

Figure 3. Bubble breakup processes in the current microchannel device: (a) Type BPO, operating condition: 0.10-0.35-0.30 (0 wt%); (b) Type BTO, operating condition: 0.20-0.35-0.30 (50 wt%); (c) The effect of Q_{up}/Q_W on the obstruction point in BTO. operating conditions from top to bottom: 0.20-0.35-0.30 (65 wt%), 0.20-0.82-0.30 (65 wt%), 0.20-1.45-0.30 (65 wt%); (d) Type NB, operating condition: 0.20-0.16-0.30 (0 wt%).

Figure 4. (a) Typical sketch of bubble breakup process for BPO. J_{up} and J_W represent the superficial upstream bubble velocity ($J_{up}=(Q_O+Q_G)/A_{CH}$) and aqueous velocity ($J_W=Q_W/A_{CH}$), respectively. (b) Evolution of bubble breakup process. Three distinct stages are divided by blue dotted lines. The operating condition is 0.10-0.35-0.30 (0 wt%).

Figure 5. (a) Independent case showing the instantaneous evolutions of the upstream and downstream bubble velocities and the aqueous phase flow rate. (b) The corresponding flow images for moments (1)-(7) in (a). The operating condition is 0.10-0.35-0.30 (0 wt%); The dotted vertical line in (a) shows the bubble breakup moment; U/J equals $U_{up}A_{CH}/(Q_O+Q_G)$ for the upstream flow and $U_{down}A_{CH}/(Q_O+Q_G+Q_W)$ for the downstream flow.

Figure 6. (a) Synchronous case showing the instantaneous evolutions of the upstream and downstream bubble velocities and the aqueous phase flow rate. (b) The corresponding flow images for moments (1)-(8) in (a). The operating condition is 0.10-0.78-0.20 (50 wt%); The dotted vertical line in (a) shows the bubble breakup moment; U/J equals $U_{up}A_{CH}/(Q_O+Q_G)$ for the

upstream flow and $U_{down}A_{CH}/(Q_O+Q_G+Q_W)$ for the downstream flow.

Figure 7. Effect of the viscosity of the aqueous phase (or glycerol concentration) on the fluctuation of the upstream and downstream bubble velocities. Q_O=0.10 mL/min, Q_G=0.35 mL/min, Q_W=0.30 mL/min. The text in the figure indicates the bubble breakup type and glycerol concentration in the aqueous phase. *U*/*J* equals $U_{up}A_{CH}/(Q_O+Q_G)$ for the upstream flow and $U_{down}A_{CH}/(Q_O+Q_G+Q_W)$ for the downstream flow.

Figure 8. Effect of the upstream flow rate on the fluctuation of the upstream and downstream bubble velocities. 30 wt% glycerol solution serves as the aqueous phase. Q_O=0.20 mL/min, Q_W=0.40 mL/min. The breakup types and Q_G are shown in the figure text. *U*/*J* equals $U_{up}A_{CH}/(Q_O+Q_G)$ for the upstream flow and $U_{down}A_{CH}/(Q_O+Q_G+Q_W)$ for the downstream flow.

Figure 9. Map of the bubble velocity variation pattern. The triangular box (II) shows the transition zone.

Figure 10. Schematic of the depression region in a typical 'obstructed' breakup regime in two-phase flow in a microfluidic T-junction according to the model of Leshansky et al.[33] The side and main channels have the same width (i.e., w_s=w).

Figure 11. Comparison of the depression region predicted by the model of Leshansky et al.[33] (i.e., Eqs. (6)-(7) in which Ca_C and J_C are replaced with Ca_W and J_W, respectively) and our experimental results. The solid lines are the experimental results and the dashed lines are obtained from the model.

Figure 12. Comparison of the predicted dimensionless bubble breakup time vs. the experimental results. Eqs. (11) and (12) are used as the models for BPO and BTO modes, respectively.

Figure 13. Simplified bubble breakup process for BPO mode (w_s=w in the current microchannel).

Figure 14. Comparison between the measured PB lengths and the predicted critical ones (Eqs. (11)-(13)). The solid and open symbols stand for data under modes BPO and BTO, respectively. The solid line represents the parity line.

Figure 15. Comparison between the predicted daughter bubble/slug lengths and the experimental results: (a) type BPO; (b) type BTO. L_{DB1}, L_{DB2}, L_{S2}, L_{S1} are predicted by Eqs. (14)-(16) and (18), respectively.

Figure 16. Comparison between our experimental results on L_{S2}/w (closed symbols) and those of literature[24] (+). Operating conditions in our experiments: the aqueous phase is deionized water, Q_W = 0.2-0.8 mL/min, Q_G = 0.28 mL/min, and Q_{up} is adjusted by the oil flow rate; Operating conditions in the literature[24]: Q_G = 0.182-0.512 mL/min, Q_O = 0.050-0.125 mL/min in the air-PEG aqueous solution-*n*-octane (with 2 wt% Span-80) system.

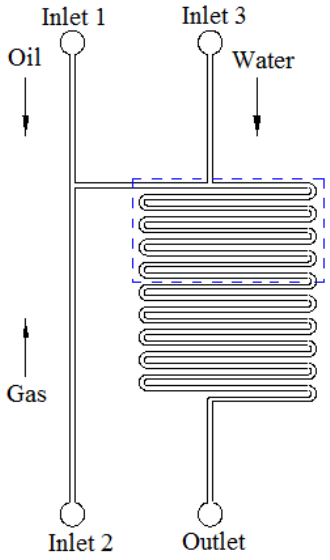

Figure 1. Schematic of the horizontally placed microchannel device with a double T-junction. The view section for camera snapshots is shown by the blue dotted box.

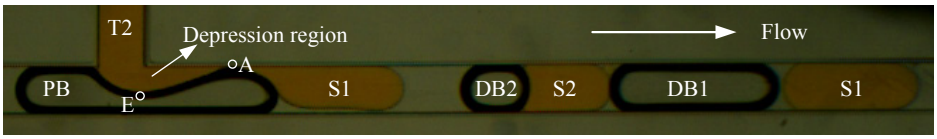

Figure 2. Important notations used in this paper. Aqueous phase is shown in orange, oil phase being the continuous carrier phase and gas bubbles being split at T2.

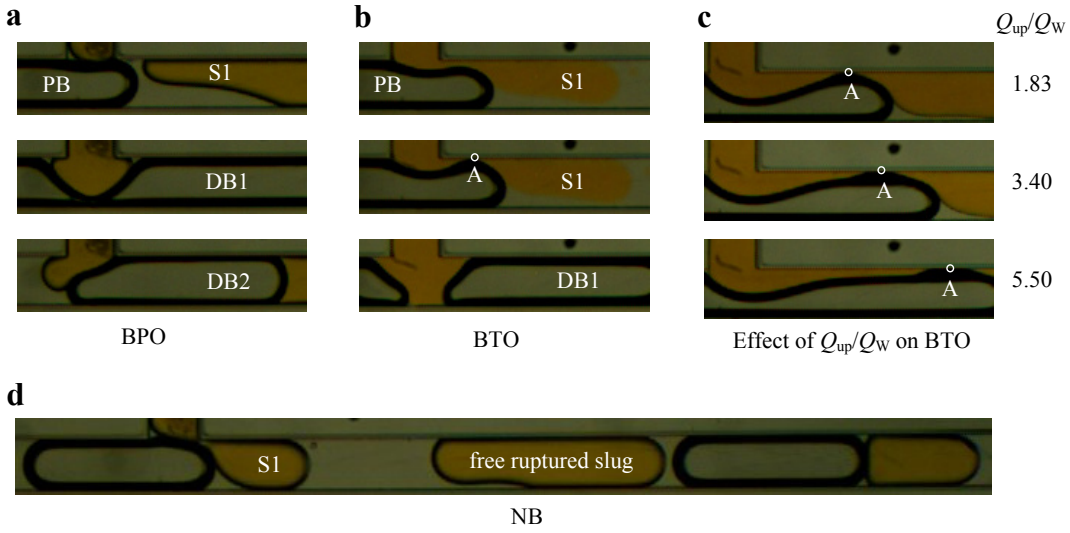

Figure 3. Bubble breakup processes in the current microchannel device: (a) Type BPO, operating condition: 0.10-0.35-0.30 (0 wt%); (b) Type BTO, operating condition: 0.20-0.35-0.30 (50 wt%); (c) The effect of Q_{up}/Q_W on the obstruction point in BTO. operating conditions from top to bottom: 0.20-0.35-0.30 (65 wt%), 0.20-0.82-0.30 (65 wt%), 0.20-1.45-0.30 (65 wt%); (d) Type NB, operating condition: 0.20-0.16-0.30 (0 wt%).

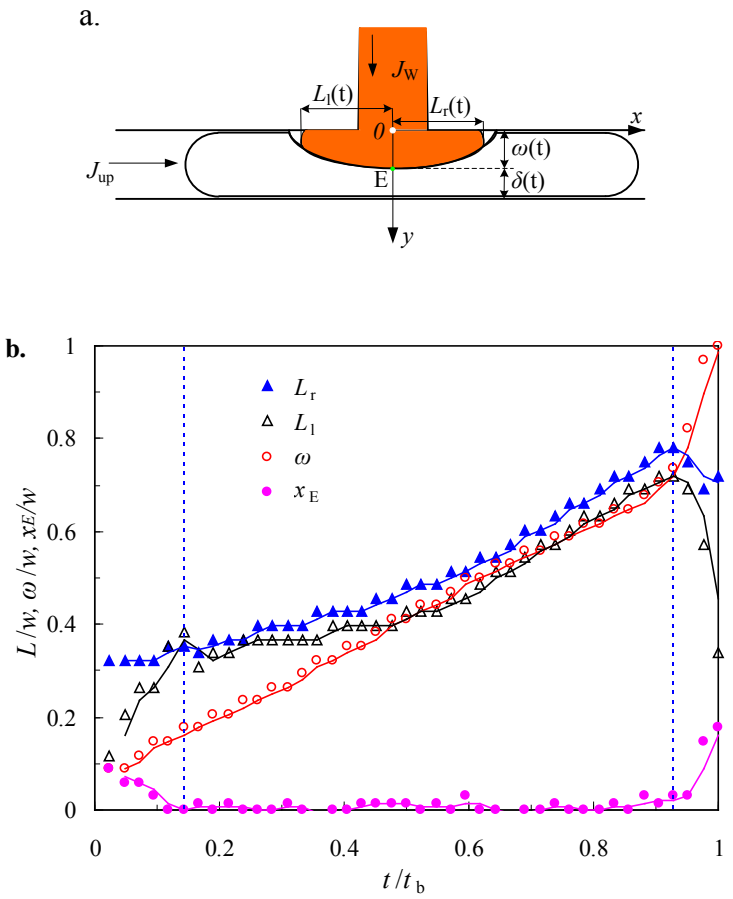

Figure 4. (a) Typical sketch of bubble breakup process for BPO. J_{up} and J_W represent the superficial upstream bubble velocity (J_{up}=(Q_O+Q_G)/A_{CH}) and aqueous velocity (J_W=Q_W/A_{CH}), respectively. (b) Evolution of bubble breakup process. Three distinct stages are divided by blue dotted lines. The operating condition is 0.10-0.35-0.30 (0 wt%).

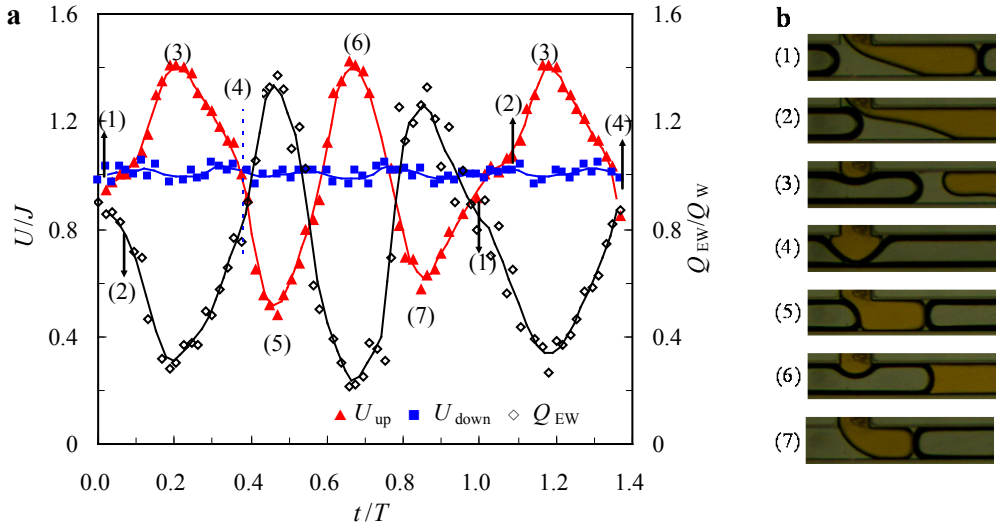

Figure 5. (a) Independent case showing the instantaneous evolutions of the upstream and downstream bubble velocities and the aqueous phase flow rate. (b) The corresponding flow images for moments (1)-(7) in (a). The operating condition is 0.10-0.35-0.30 (0 wt%); The dotted vertical line in (a) shows the bubble breakup moment; U/J equals $U_{up}A_{CH}/(Q_O+Q_G)$ for the upstream flow and $U_{down}A_{CH}/(Q_O+Q_G+Q_W)$ for the downstream flow.

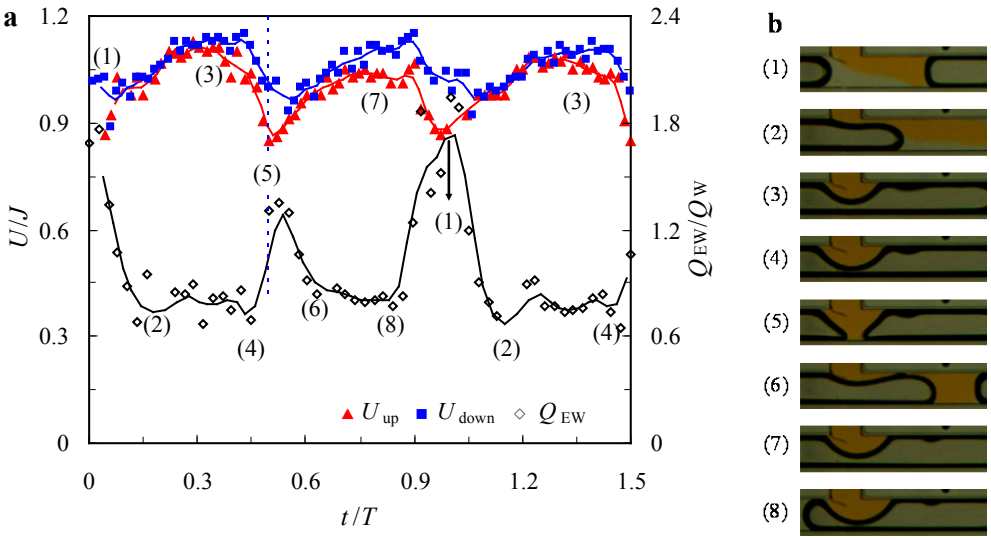

Figure 6. (a) Synchronous case showing the instantaneous evolutions of the upstream and downstream bubble velocities and the aqueous phase flow rate. (b) The corresponding flow images for moments (1)-(8) in (a). The operating condition is 0.10-0.78-0.20 (50 wt%); The dotted vertical line in (a) shows the bubble breakup moment; U/J equals $U_{up}A_{CH}/(Q_O+Q_G)$ for the upstream flow and $U_{down}A_{CH}/(Q_O+Q_G+Q_W)$ for the downstream flow.

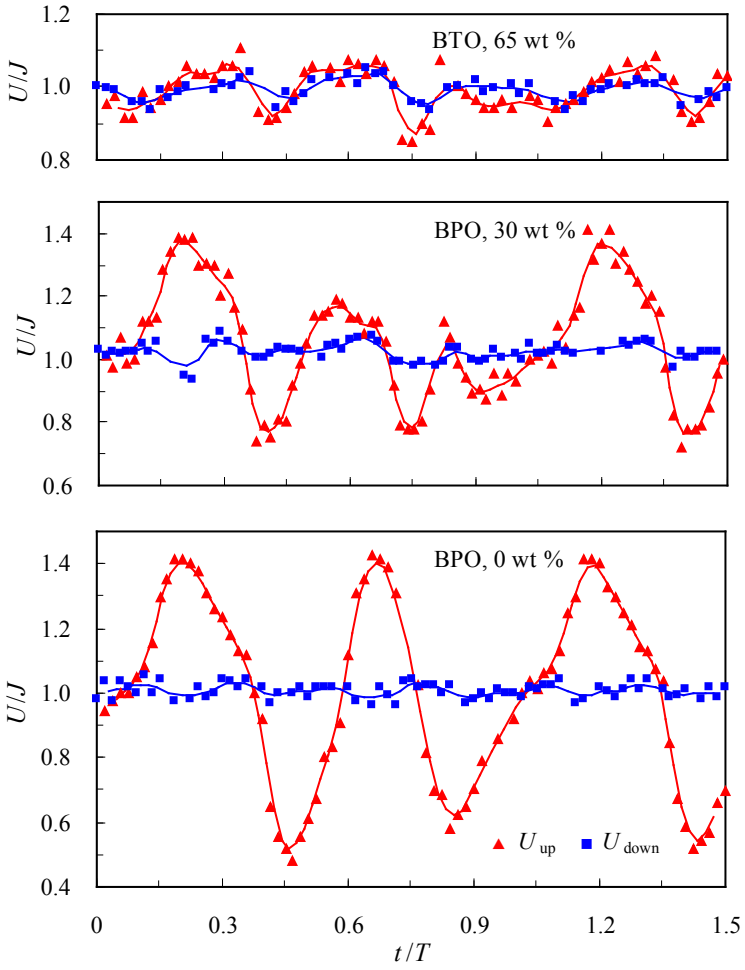

Figure 7. Effect of the viscosity of the aqueous phase (or glycerol concentration) on the fluctuation of the upstream and downstream bubble velocities. Q_O=0.10 mL/min, Q_G=0.35 mL/min, Q_W=0.30 mL/min. The text in the figure indicates the bubble breakup type and glycerol concentration in the aqueous phase. U/J equals $U_{up}A_{CH}/(Q_O+Q_G)$ for the upstream flow and $U_{down}A_{CH}/(Q_O+Q_G+Q_W)$ for the downstream flow.

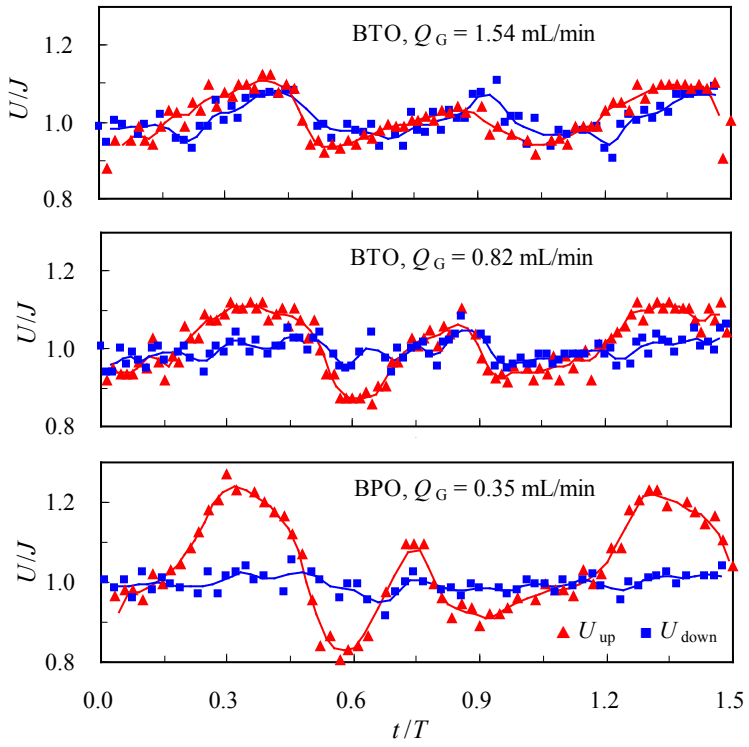

Figure 8. Effect of the upstream flow rate on the fluctuation of the upstream and downstream bubble velocities. 30 wt% glycerol solution serves as the aqueous phase. Q_O=0.20 mL/min, Q_W=0.40 mL/min. The breakup types and Q_G are shown in the figure text. U/J equals $U_{up}A_{CH}/(Q_O+Q_G)$ for the upstream flow and $U_{down}A_{CH}/(Q_O+Q_G+Q_W)$ for the downstream flow.

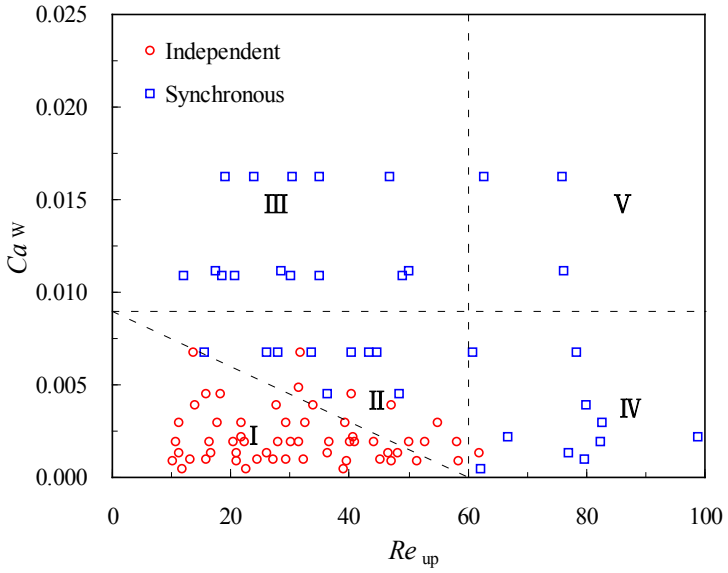

Figure 9. Map of the bubble velocity variation pattern. The triangular box (II) shows the transition zone.

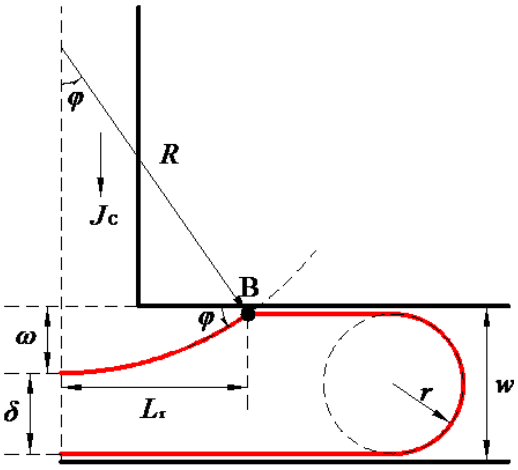

Figure 10. Schematic of the depression region in a typical 'obstructed' breakup regime in two-phase flow in a microfluidic T-junction according to the model of Leshansky et al.[33] The side and main channels have the same width (i.e., w_s=w).

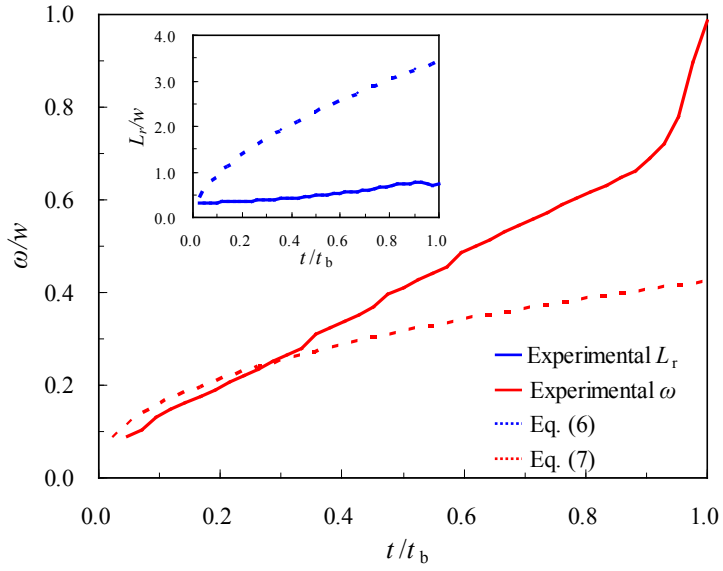

Figure 11. Comparison of the depression region predicted by the model of Leshansky et al.[33] (i.e., Eqs. (6)-(7) in which Ca_C and J_C are replaced with Ca_W and J_W, respectively) and our experimental results. The solid lines are the experimental results and the dashed lines are obtained from the model.

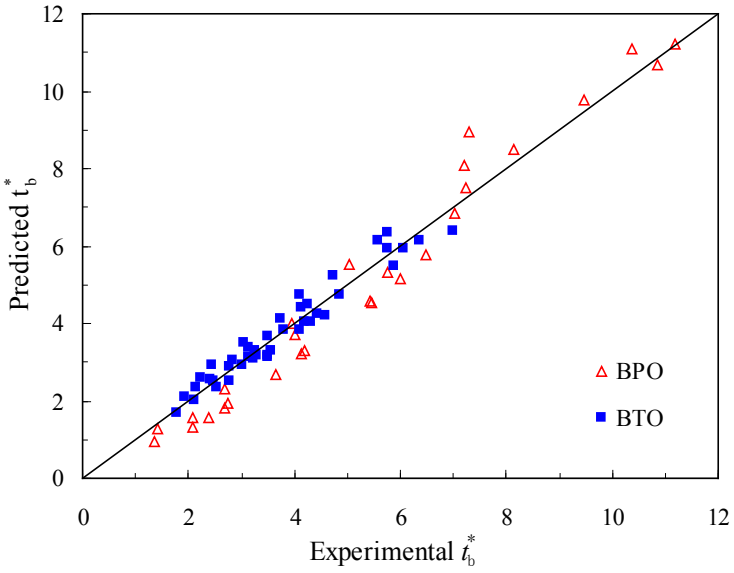

Figure 12. Comparison of the predicted dimensionless bubble breakup time vs. the experimental results. Eqs. (11) and (12) are used as the models for BPO and BTO modes, respectively.

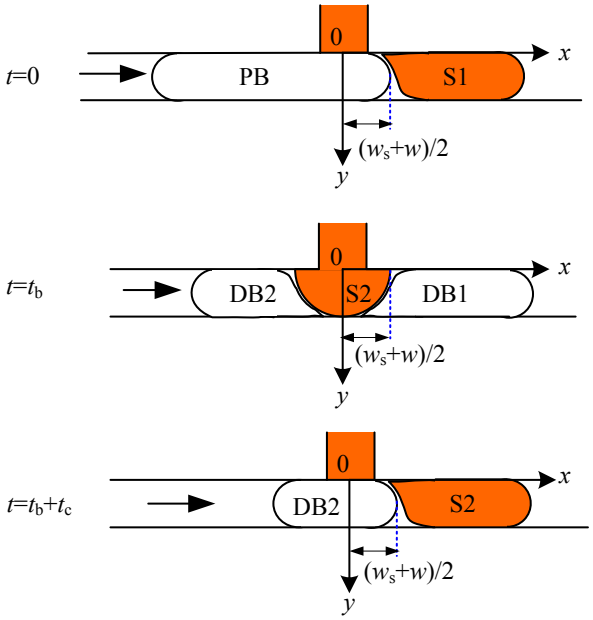

Figure 13. Simplified bubble breakup process for BPO mode (w_s=w in the current microchannel).

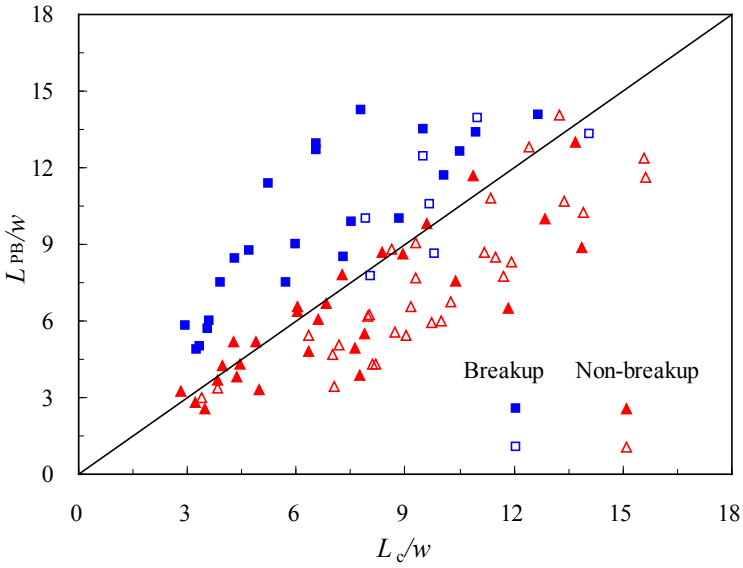

Figure 14. Comparison between the measured PB lengths and the predicted critical ones (with Eqs. (11)-(13)). The solid and open symbols stand for data under BPO and BTO modes, respectively. The solid line represents the parity line.

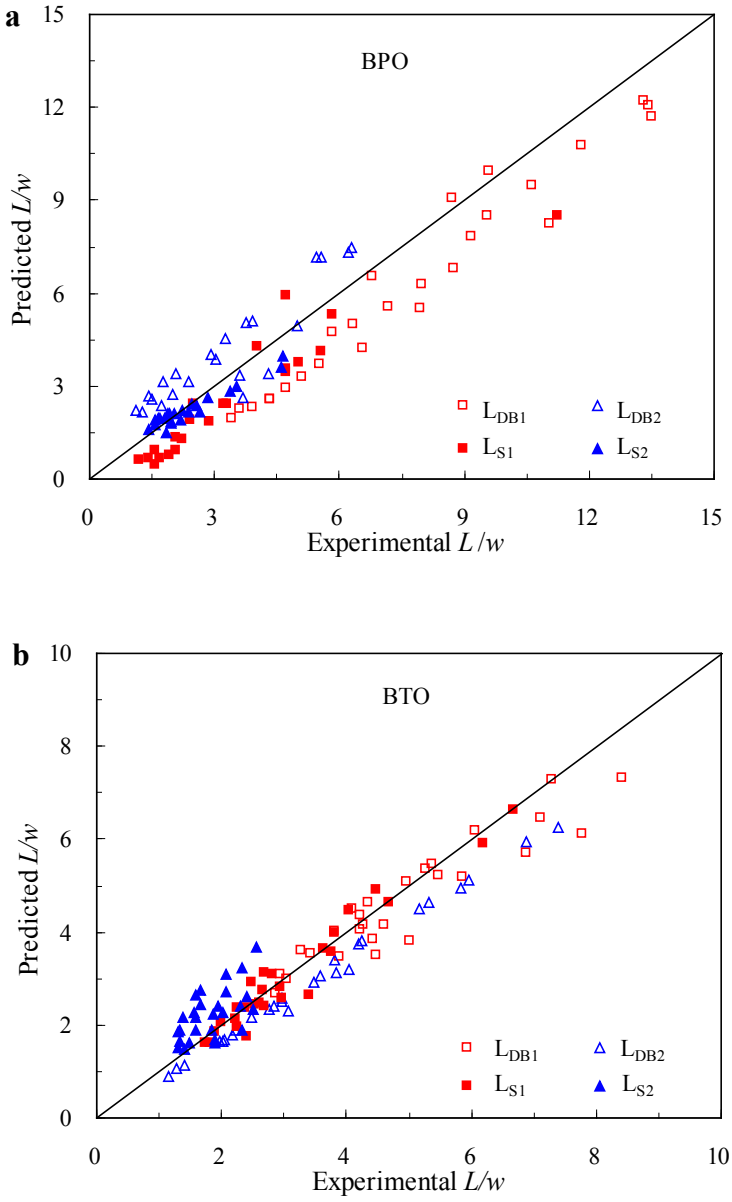

Figure 15. Comparison between the predicted daughter bubble/slug lengths and the experimental results: (a) type BPO; (b) type BTO. L_{DB1}, L_{DB2}, L_{S2}, L_{S1} are predicted by Eqs. (14)-(16) and (18), respectively.

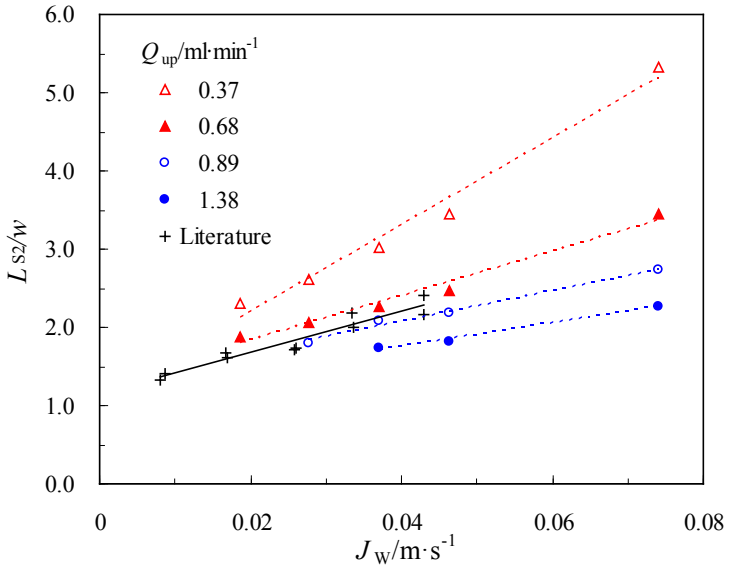

Figure 16. Comparison between our experimental results on L_{S2}/w (closed symbols) and those of literature[24] (+). Operating conditions in our experiments: the aqueous phase is deionized water, Q_W = 0.2-0.8 mL/min, Q_G = 0.28 mL/min, and Q_{up} is adjusted by the oil flow rate; Operating conditions in the literature[24]: Q_G = 0.182-0.512 mL/min, Q_O = 0.050-0.125 mL/min in the air-PEG aqueous solution-*n*-octane (with 2 wt% Span-80) system.